Compressive deformation of as-extruded LPSO-containing Mg alloys at different temperatures

Zhao, Di; Zhao, Chaoyue; Chen, Xianhua; Huang, Yuanding; Hort, Norbert; Gavras, Sarkis; Pan, Fusheng

Published in:
Journal of Materials Research and Technology

DOI:
10.1016/j.jmrt.2021.12.053

Publication date:
2022

Document Version
Publisher's PDF, also known as Version of record

Available online at www.sciencedirect.com

jmr&t Journal of Materials Research and Technology

journal homepage: www.elsevier.com/locate/jmrt

Original Article

Compressive deformation of as-extruded LPSO-containing Mg alloys at different temperatures

Di Zhao [a], Chaoyue Zhao [a], Xianhua Chen [a,b,c,*], Yuanding Huang [c], Norbert Hort [c,d], Sarkis Gavras [c], Fusheng Pan [a,b]

[a] International Joint Laboratory for Light Alloys (MOE), College of Materials Science and Engineering, Chongqing University, Chongqing, 400045, China

[b] National Engineering Research Center for Magnesium Alloys, Chongqing University, Chongqing 400045, China

[c] Institute of Metallic Biomaterials, Helmholtz-Zentrum Hereon, Max-Planck-Straße 1, D-21502, Geesthacht, Germany

[d] Institute of Product and Process Innovation, Leuphana University Lüneburg, Universitätsallee 1, D-21335, Lüneburg, Germany

ARTICLE INFO

Article history:
Received 8 November 2021
Accepted 10 December 2021
Available online 16 December 2021

Keywords:
LPSO phase
Strain hardening
Dynamic recrystallization
Hot deformation
Constitutive equation
DRX Kinetic model

ABSTRACT

This work investigates the compressive deformation behavior of as-extruded Mg-6Gd-1.6Y−1Zn-0.4Zr (VZ61) and Mg-6Gd-4.8Y−3Zn-0.4Zr (VZ63) alloys via uniaxial compressive tests at various deformation temperatures. At room temperature, compared with the VZ61 alloy, the compressive yield strength of the VZ63 alloy were obviously enhanced due to its increased amount of LPSO phase. Both alloys exhibited a three-stage strain hardening feature. The strain hardening rate first sharply decreases (stage I), then continues to increase at a slower rate (stage II) and finally decreases (stage III). At stage III, a larger number of dislocation accumulation around the kinked LPSO phase resulted in a higher strain hardening rate for VZ63 alloy than that for VZ61 alloy. During high temperature compression, the true stress−strain curves showed that the flow stress gradually reduced with increasing temperature and also the reducing of strain rate, and the VZ63 alloy displayed a higher peak stress than VZ61 alloy. Constitutive equations were constructed based on the true stress−strain to better understand the relation among flow tress (σ), strain rate ($\dot{\varepsilon}$) and deformation temperature (T) in VZ alloys during hot deformation. The results showed that the VZ63 alloy had a lower deformation activation energy (Q = 255.6 kJ/mol) than VZ61 alloy (Q = 395.5 kJ/mol). The DRX kinetic models of the VZ61 and VZ63 alloys were also established, indicating that the VZ63 alloy was more prone to DRX with a higher volume fraction of dynamically recrystallized grains (XDRX) at the same deformation conditions.

* Corresponding author.
E-mail address: xhchen@cqu.edu.cn (X. Chen).

https://doi.org/10.1016/j.jmrt.2021.12.053

1. Introduction

Magnesium (Mg) alloys are widely used due to their low density and excellent specific properties, which are regarded as ideal engineering materials [1,2]. Nevertheless, application fields of Mg alloys are enormously limited due to their poor strength, ductility and formability at room and high temperature [3,4]. Some important efforts were devoted to overcome these limitations by such processing techniques as plastic deformation and alloying [5–7]. For example, extrusion or hot rolling can effectively eliminate casting defects and refine microstructure, and enhance the strength of Mg alloys [8,9]. These plastic deformation technologies can also control the texture of Mg alloys to improve the ductility and the stretch formability [9]. In addition, the addition of alloy elements, especially rare-earth (RE) elements, was a promising way to improve the mechanical properties of Mg alloys by precipitate strengthening, changing the basal texture [10,11]. Among all kinds of Mg-RE alloys, Mg–Gd/Y–Zn alloys have drawn extensive attention due to their good mechanical properties at room temperature [12–15]. Generally, the phases formed in the Mg–Gd/Y–Zn alloys can be classified into three types based on their structures [16,17]:

- long-period stacking ordered (LPSO) phase,
- cubic phase (W phase, $Mg_3Zn_3Y_2$), and
- icosahedral quasi-crystal phase (I phase, $Mg_3Zn_6Y_2$).

Among them, LPSO phase can strengthen Mg alloys more effectively, since it exhibits greater hardness, elastic modulus and thermal stability [18–20]. Moreover, it can improve critical resolved shear stress (CRSS) of basal slip, produce deformation-kinking and influence DRX process. All of these play a major role in enhancing the mechanical properties of LPSO-containing Mg alloys [21–25]. Wang et al. [26] prepared Mg-8.8Gd-3.4Y–1Zn-0.8Mn (wt. %) alloy sheets with a yield strength of 318 MPa and ultimate strength of 434 MPa using a large-strain high-efficiency rolling process. Yamasaki et al. [27] developed an extruded $Mg_{96.5}Zn_1Gd_{2.5}$ (at.%) alloy with highly dispersed LPSO phase possessing excellent yield strength of 345 MPa and elongation of 6.9%. The $Mg_{97}Zn_1Y_2$ (at. %) alloy with a yield strength (TYS) of 610 MPa and elongation (EL) of 5% at room temperature was prepared by a rapidly solidified powder metallurgy process. Its high yield strength was related to the lamellar LPSO phase and nano grains [28]. Although the production of LPSO phase is beneficial for the enhanced mechanical properties of Mg alloys [29], to the best of our knowledge, there is still lack of a systematical study on the influence of LPSO fraction on compressive deformation at room temperature.

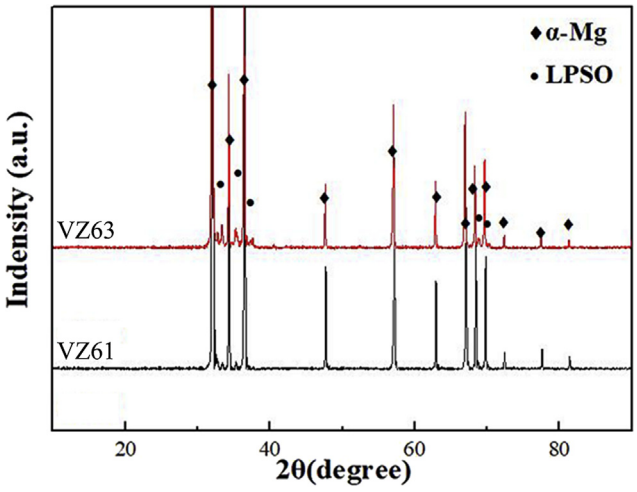

Fig. 1 – XRD patterns of VZ61 and VZ63 alloy.

In addition to good room temperature mechanical properties, modern industrial applications also require high temperature mechanical properties of materials. Unfortunately, Mg alloys are prone to softening at elevated temperatures due to their DRX propensity, activation of non-basal slip and unstable microstructure [30–32]. AZ91D, AM50A and AM60B alloys do not have sufficient strength above 125 °C for certain industrial applications [33]. The second phases in such alloys have a low thermal stability [31,34]. In contrast, the strength of LPSO-containing Mg alloys at high temperatures is much higher than that of commercial Mg alloys [35,36]. Moreover, Mg alloys containing LPSO phase displayed an outstanding deformability up to 60% of maximum compression strain at high temperatures, which was attributed to the combinative effects of kinked LPSO phase and other deformation mechanisms [25,37]. Considering these advantages, further investigation on the effects of LPSO phase on the hot deformation of magnesium alloys was performed. Li et al. [24] developed the Mg-Gd-Zn alloys with LPSO phase and investigated their hot deformation and DRX behavior, indicating that the flow stress reduced with increasing the deformation temperature and decreasing strain rate due to DRX softening. Furthermore, they also found that large angle kink band boundaries induced DRX, while the LPSO phase impeded the occurrence of DRX. Chen et al. [38] investigated the microstructural evolution of Mg–Y–Zn alloy by focusing on DRX under different deformation conditions. The results showed that kinked areas could act as the nucleation sites for initial DRX. The boundary migration of DRX grains could be pinned by the LPSO phase. However, until now, it is not clear how the fraction of LPSO phase affects the DRX and flow stress of Mg alloys. Further identification of the relationship between the flow behavior of LPSO-containing Mg alloys and deformation parameters such as temperature and stain rate is required. In this work, the effects of the LPSO phase fraction on the compressive deformation behavior for Mg-6Gd-1.6Y–Zn-0.4Zr and Mg-6Gd-4.8Y–3Zn-0.4Zr alloys at various temperatures is investigated using uniaxial compressive tests. A constitutive equation and the DRX kinetic model is established according to the data analysis of hot deformation.

2. Experimental

Commercially pure Mg (99.8 wt%), Mg-30Gd (wt. %), Mg–30Y (wt. %), pure Zn and pure Zr were used to prepare the ingots of Mg-6Gd-1.6Y–Zn-0.4Zr (VZ61 alloy) and Mg-6Gd-4.8Y–3Zn-0.4Zr (VZ63 alloy). These master alloys were put into a crucible (⌀ 90 × 270 mm) and melted using a vacuum induction furnace under the protection of Ar gas. The as-cast ingots were cut

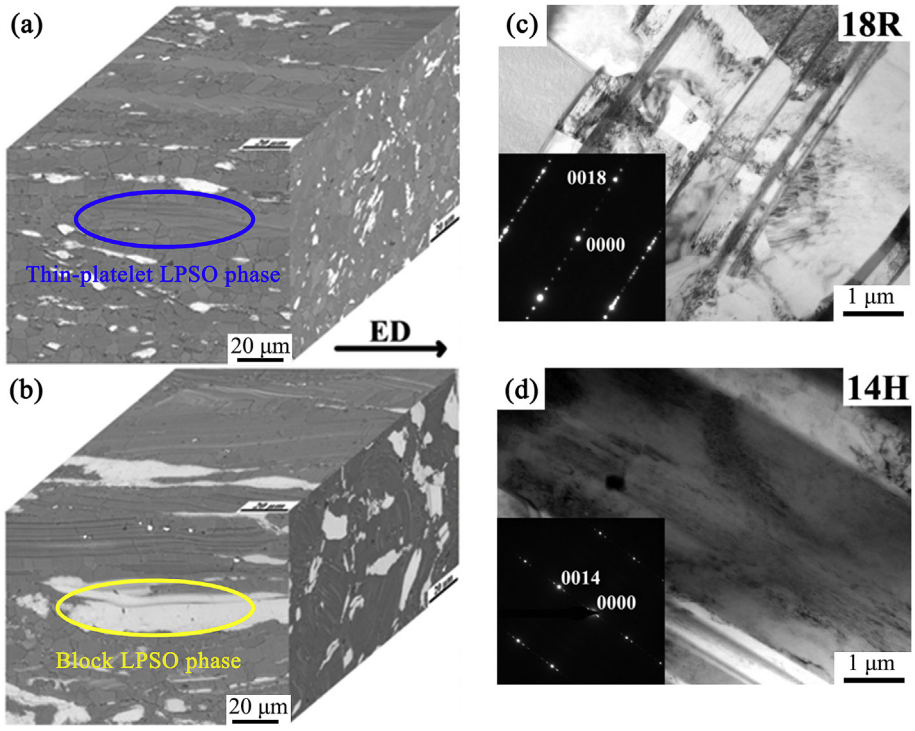

Fig. 2 – SEM micrographs of VZ61 alloy (a) and VZ63 alloy (b). Bright-field TEM micrographs with corresponding SAED patterns of thin-platelet LPSO phase (c) and block LPSO phase (d).

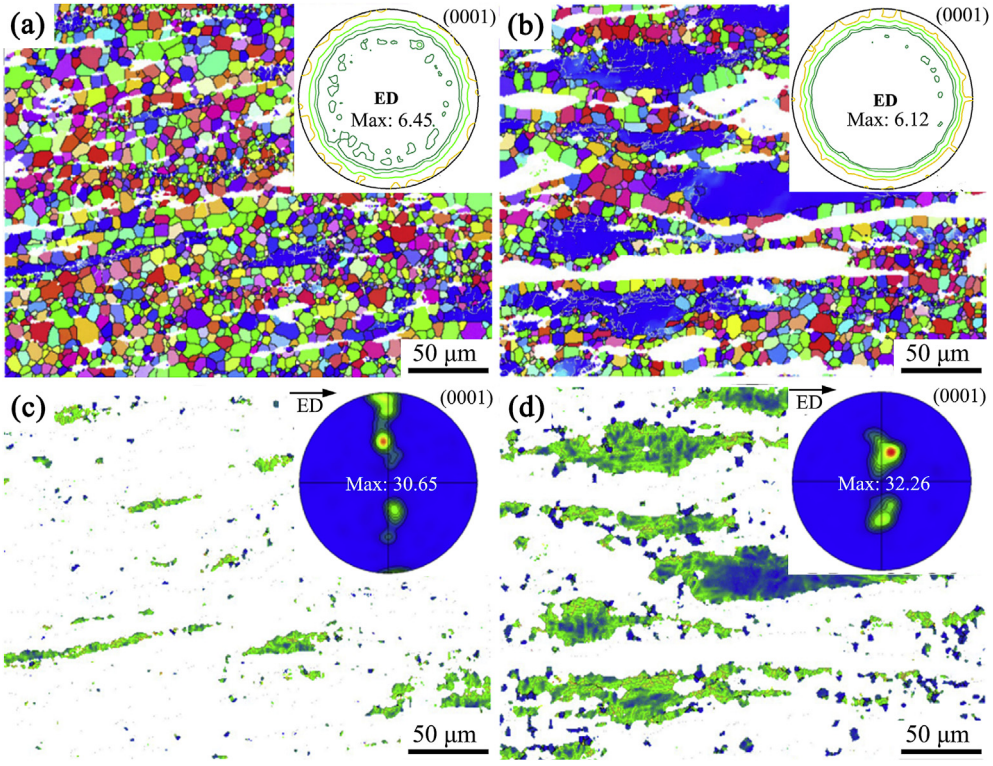

Fig. 3 – EBSD inverse pole figures and texture of as-extruded VZ series alloys: (a) and (c) VZ61 alloy, (b) and (d) VZ63 alloy, (c) unrecrystallized regions in VZ61 alloy, (d) unrecrystallized regions in VZ63 alloy.

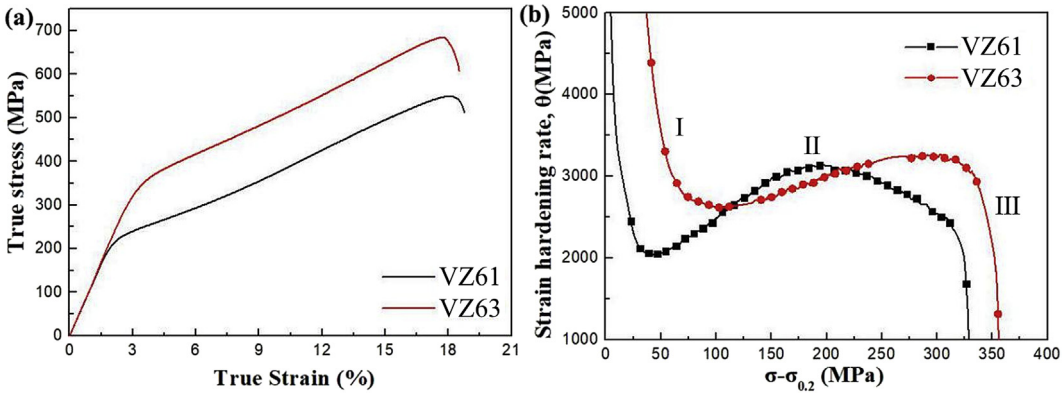

Fig. 4 – True compressive stress–strain (a) and strain-hardening (b) curves for the as-extruded samples.

into cylindrical specimens (⌀ 80 × 60 mm), and then homogenized at 540 °C for 4 h for subsequent extrusion. The extrusion process was carried out at 430 °C on a XJ-500 Horizontal Extrusion Machine with an extrusion ratio of 10:1. Compressive samples cut from extrusion bars were machined into a diameter of 8 mm and a gauge length of 12 mm. Room-temperature compressive tests were carried out on a CMT5105 material testing machine with a strain rate of 10^{-3} s^{-1}. Hot compressive tests were carried out at 250 °C, 300 °C, and 350 °C on Gleeble-3500D thermal simulation testing machine. The strain rates were set as 0.001 s^{-1}, 0.01 s^{-1} and 0.1 s^{-1}, respectively. A Rigaku D/MAX-2500PC X-ray diffractometer (XRD) was used to identify secondary phases and analyze macro texture. The microstructures of alloys were characterized by a scanning electron microcopy (SEM, JEOL JSM-7800F FEG) and a transmission electron microscopy (TEM, JEM-2100). Specimens for SEM were etched in a mixture of a 5 ml acetic acid, 10 ml water and 50 ml ethanol with picric acid added to saturation for about 30 s. Electron back-scatter diffraction (EBSD) data were also obtained by SEM equipped with the HKL EBSD system. The step size for the specimens before and after deformation were 1 μm and 0.6 μm, respectively. The samples for EBSD were polished by a Gatan II ion + II 697 argon ion instrument. Thin foil samples for TEM were ion-beam thinned using a Gatan 695 Ion Polishing System at −70 °C for 1.5–2 h. The ion beam energy and angle were first 6 keV and 6°, respectively, and then adjusted to 2 keV and 2° after producing a small hole.

3. Results and discussion

3.1. Compression behavior at room temperature

3.1.1. Microstructure characterizations

Figure 1 displays the XRD patterns of extruded VZ series alloys. Both of the extruded VZ61 and VZ63 alloys include the α-Mg and LPSO phase. Figure 2 exhibits the microstructures of extruded VZ alloys. In Fig. 2a and b, the grayish white phases are distributed along ED in the α-Mg matrix. With the increase of Zn content, the volume fraction of these phases increases. Combined with XRD results, these particles were identified as LPSO phases including two kinds of microscopic morphology: thin-platelet LPSO phase and block LPSO phase. The volume fraction of block LPSO phases is much higher than that of thin-platelet ones, especially for the VZ63 alloy. The TEM images with the corresponding SAED patterns in Fig. 2c-e indicate that the thin-platelet LPSO phase has 18R structure (Fig. 2c) and the block LPSO phase has 14H structure (Fig. 2d). Additionally, few cuboidal particles were observed in the alloys.

Based on the EBSD results (Fig. 3), both of the extruded VZ61 (Fig. 3a and c) and VZ63 alloys (Fig. 3b and d) exhibit a classic bimodal grain structure with fine dynamic recrystallized (DRXed) grains and large deformed grains elongated along the extrusion direction (ED). The size of DRXed grains is nearly 5 μm and hardly changes with increasing Zn content. However, the volume fraction of un-DRX area increases from 5.6% for the VZ61 alloy to 27.2% for the VZ63 alloy. In addition, both of the extruded VZ61 and VZ63 alloys show a typical fiber texture with c-axis perpendicular to ED. They have the similar maximum pole intensity. Compared with the VZ63 alloy, the extruded VZ61 alloy has fewer deformed grains, as showni in Fig. 3c and d. Thus, the extruded VZ61 alloy displays more random grain orientation than the extruded VZ63 alloy, which is related to its high DRX fraction.

3.1.2. Compressive stress–strain behavior

Figure 4a presents the true compressive stress–strain curves of extruded VZ series alloys at room temperature. Their corresponding compressive properties consisting of ultimate compressive strength (σ_{UCS}), compressive yield strength ($\sigma_{0.2}$), elongation-to-failure (ε_f) and uniform strain (ε_p) are listed in Table 1. With increasing Zn content, the compressive strength and yield strength are improved from ~ 548 to ~ 648 MPa and from ~ 219 to ~ 348 MPa, respectively, while their elongation-to-fracture remains similar. As is known, the

Table 1 – Ultimate compressive strength (σ_{UCS}), compressive yield strength ($\sigma_{0.2}$), elongation-to-failure (ε_f) and uniform strain (ε_p) of the as-extruded VZ series alloys.

Alloy	σ_{UCS} (MPa)	$\sigma_{0.2}$ (MPa)	ε_f (%)	ε_p (%)
VZ61	548	219	18.7	14.0
VZ63	648	348	18.5	13.2

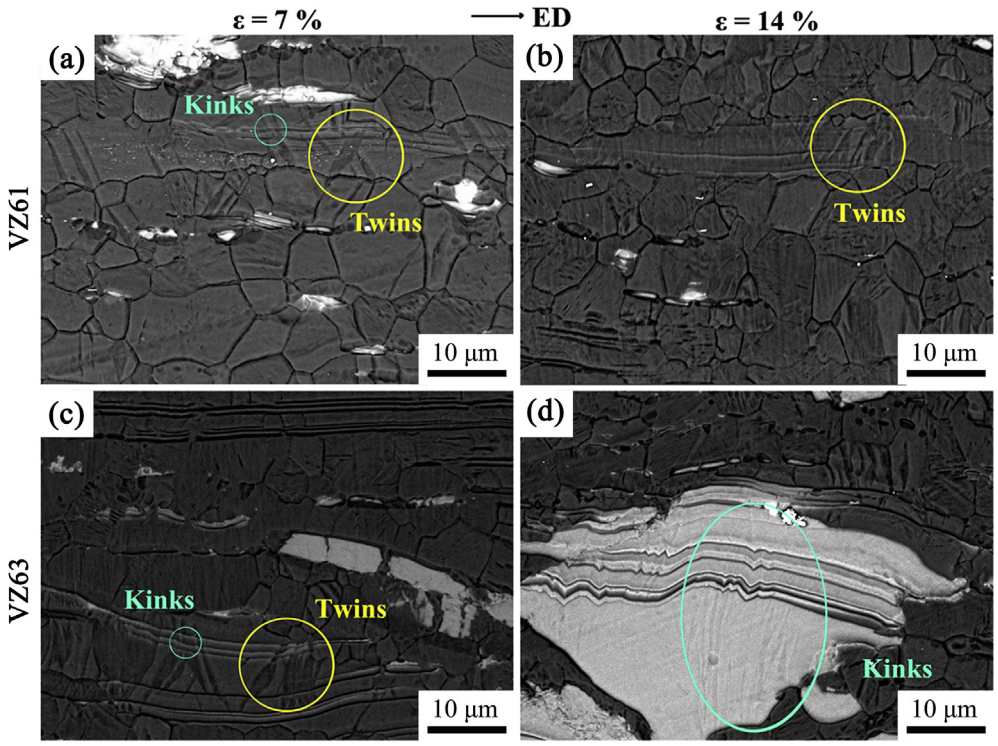

Fig. 5 – SEM-BSE micrographs of as-extruded VZ alloys after compressive deformation at room temperature: ε = 7%, (a) VZ61, (c) VZ63; ε = 14%, (b) VZ61, (d) VZ63.

strength of alloys can be improved if the dislocation movement is hindered. Figure 5 shows the SEM-BSE (Backscattering) of extruded VZ alloys subjected to the deformation with compressive strains of 7% and 14% at room temperature. With the increase of deformation, the LPSO phase began to have a clear kink deformation form, marked by cyan ellipses. As shown in Fig. 6, numerous dislocations (marked by blue line frame) are accumulated around the kinked LPSO phases, demonstrating that the kink boundaries can hinder dislocation movement, thereby leading to the significant increase in the strength of VZ63 alloy with more LPSO phase.

The strain hardening behaviors of extruded VZ alloys are described by the strain hardening rate θ [39,40]:

$$\theta = d\sigma/d\varepsilon \quad (1)$$

Where σ and ε are the true stress and plastic strain, respectively.

Figure 4b shows the strain-hardening curves of extruded VZ alloys during compression at room temperature. The whole compression process mainly includes three different stages that are referred to as I, II and III. Stage I, at the beginning of compression, displays a sharp decrease in the strain hardening rate, which is owing to a short elastoplastic transition. Then, at stage II, the strain hardening rate reaches a peak value of 3134 MPa at $(\sigma\text{-}\sigma_{0.2}) = 195$ MPa for the VZ61 alloy and 3249 MPa at $(\sigma\text{-}\sigma_{0.2}) = 276$ MPa for the VZ63 alloy. As the $(\sigma\text{-}\sigma_{0.2})$ increases from ~ 113 to ~ 223 MPa, the strain hardening rate of extruded VZ61 alloy is larger than that of extruded VZ63 alloy, which is related to twinning. Previous investigations reported that the appearance of stage II is ascribed to the twin-dislocation interactions, since twin boundaries can act as strong obstructions to prevent dislocation movement, leading to dislocations pileup, thereby improving the strain hardening rate [41–43].

After compressive deformation, in both of the extruded VZ61 and VZ63 alloys, the {10 $\bar{1}$ 2} ension twinning (red line) is dominant as shown in Fig. 7. With the increase of the deformation strain from 7% (Fig. 7a and c) to 14% (Fig. 7b and d), the volume fraction of twins increases from ~ 7.91 to ~ 8.26% in the extruded VZ61 alloy (Fig. 7a and b) and from ~ 3.93 to ~ 5.15% in the extruded VZ63 alloy (Fig. 7c and d), respectively. Moreover, the volume fraction of twins in the extruded VZ61 alloy is obviously higher than that in the extruded VZ63 alloy. Therefore, at stage II, with the $(\sigma\text{-}\sigma_{0.2})$ increased from ~ 113 to ~ 223 MPa, the strain hardening rate of extruded VZ61 alloy is larger than that of extruded VZ63 alloy owing to the existence of more twins.

With further compression, the strain hardening rate sharply decreases at stage III until failure, which is attributed to the lack of twins impeding dislocation slip [44]. The decrease of the strain hardening rate in VZ63 alloy is less than that of in VZ61 alloy, that is, the VZ63 alloy exhibits a higher strain hardening rate than VZ61 alloy at stage III. Generally, stage III is associated with the annihilation of dislocations. More kinked LPSO phase in VZ63 alloy can effectively hinder the dislocation movement and increase the dislocation density (Fig. 6), which results in VZ63 alloy bearing greater external stress and improving the deformation resistance.

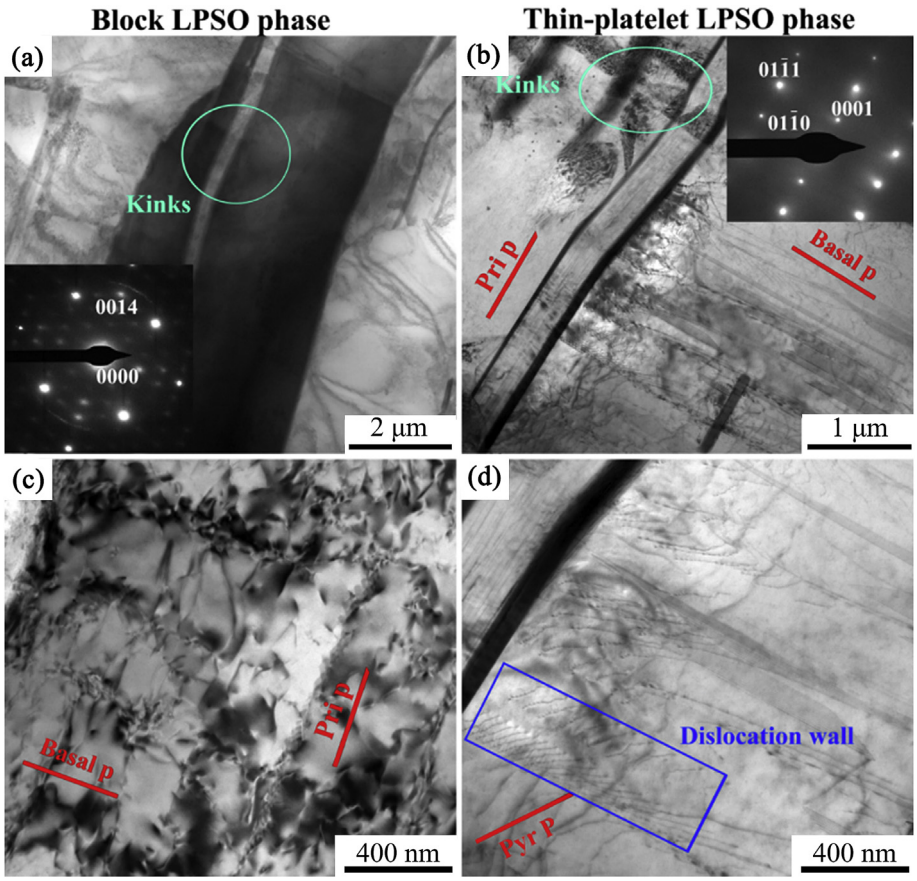

Fig. 6 – TEM micrographs and selected area diffraction patterns of LPSO phase in the as-extruded VZ63 alloy after compressive deformation with a strain of 14%: (a, b) block LPSO phase, (c, d) thin-platelet LPSO phase. "Basal p", "Pri p" and "Pyr p" represent basal plane, prismatic plane and pyramidal plane, respectively.

Consequently, at stage III, VZ63 alloy exhibits a higher strain hardening rate than VZ61 alloy.

3.2. *Compression behavior at elevated temperatures*

3.2.1. *Microstructural characterizations*

Figures 8 and 9 display the SEM micrographs of extruded VZ alloys subjected to compression at various temperatures and strain rates. At low temperatures and low strain rates, both of the extruded VZ61 and VZ63 alloys mainly include large deformed grains. Only a few of the DRXed grains are present at grain boundaries. When rising the deformation temperature and reducing the strain rate, the volume fraction of DRXed grains gradually increases, accompanied with a "necklace structure" along the deformed grain boundaries (yellow circle in Fig. 8). In the VZ63 alloy after compression, the LPSO particles exhibit obvious kink deformation (yellow circles in Fig. 9). In addition to the deformed grain boundary, fewer DRXed grains are also distributed along kink boundaries (KBs) of LPSO phase. They gradually increase with the increase of temperature and the reduction of stain rate.

Figure 10 displays the microstructural characteristics and texture of VZ alloys after compression under different deformation conditions. The tensile twin almost disappears during high temperature compression, indicating that dislocation slip is the main deformation mode. At 250 °C (Fig. 10a and c), the (0001) plane of most grains in VZ alloys is perpendicular to the compression direction. The texture intensity of VZ61 and VZ63 alloys is 9.58 and 6.01, respectively. When the temperature rises to 350 °C (Fig. 10b and d), the grains are obviously refined. The dynamic recrystallization occurred in VZ61 and VZ63 alloys accompanied with the weaker texture. Compared with the VZ61 alloy, the VZ63 alloy exhibits a smaller grain size, since the migration of DRXed grain boundaries can be pinned by LPSO phase [21].

3.2.2. *Flow behavior*

The true compressive strain–stress curves of as-extruded VZ alloys under various strain rates and deformation temperatures are shown in Fig. 11. They display similar deformation characteristics at various conditions, i.e. three stages: hardening stage, transition stage and softening stage [45]. At the early stage of deformation, the flow stress rapidly increases with increasing the strain owing to the strain hardening introduced by the increase of dislocation density [38]. At the transition stage, with the compressive deformation increasing to the critical strain, DRX occurred. Since the enhancement of dynamic softening partially offsets the

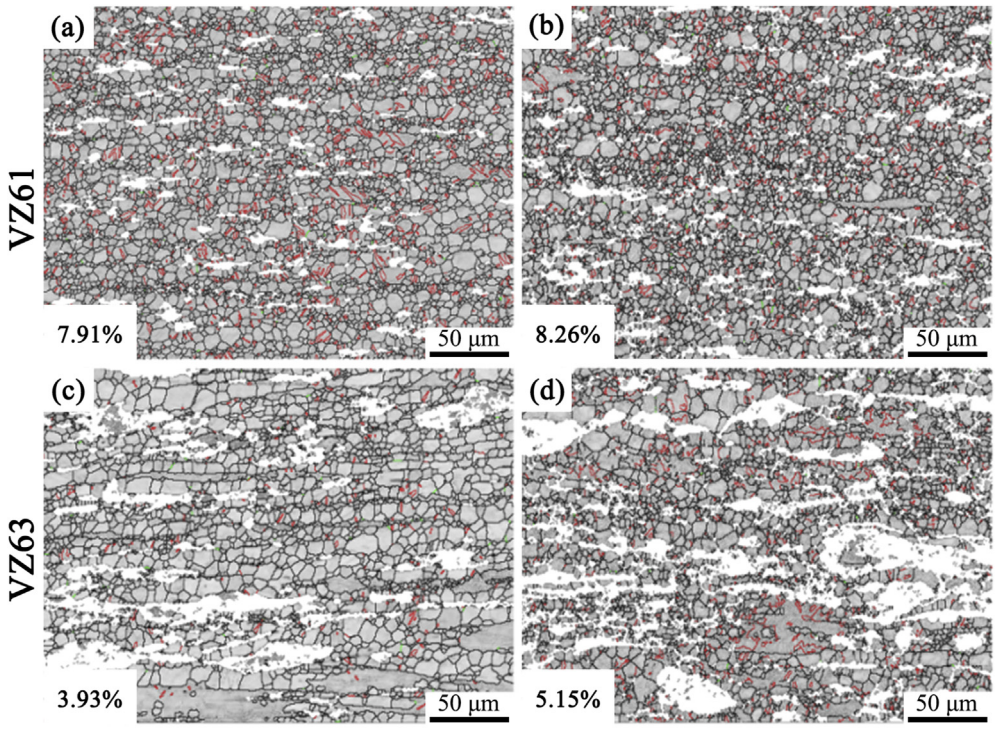

Fig. 7 – Grain boundary maps of as-extruded VZ alloys after compression at room temperature: ε = 7%, (a) VZ61, (c) VZ63; ε = 14%, (b) VZ61, (d) VZ63. {10 $\bar{1}$ 2} tension twin and {10 $\bar{1}$ 1} compression twin are represented by red and green line.

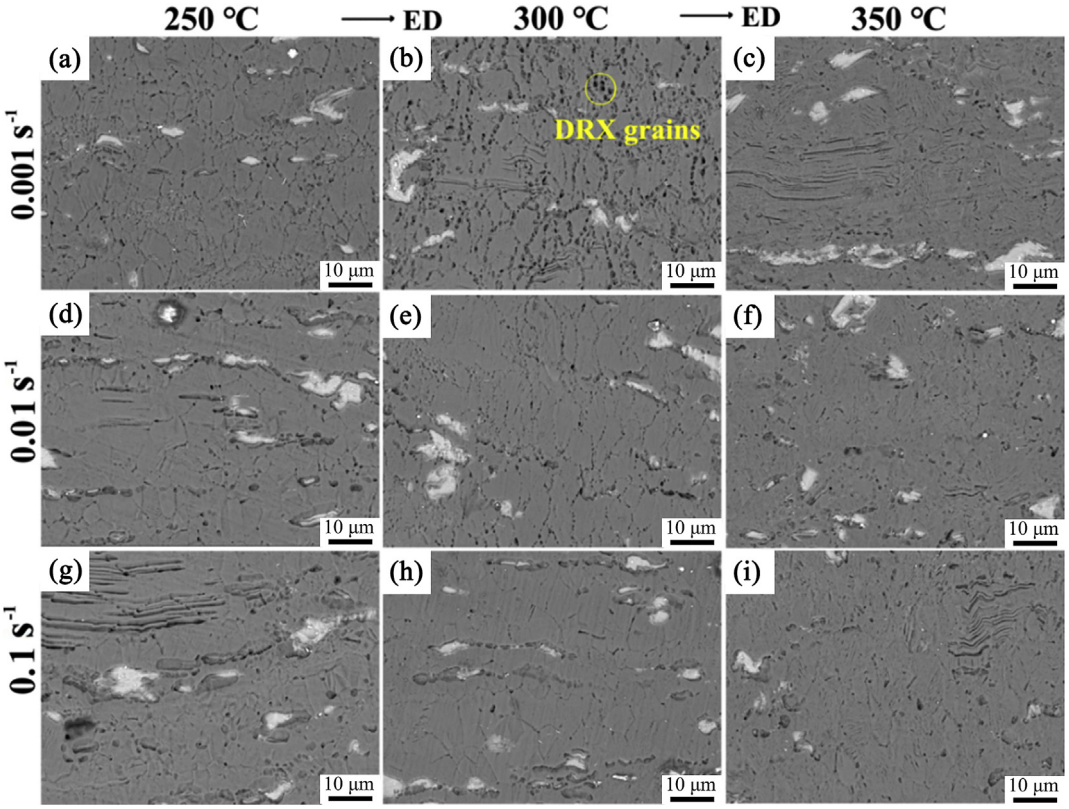

Fig. 8 – SEM micrographsof VZ61 alloy after compressive deformations at various temperatures and strain rates.

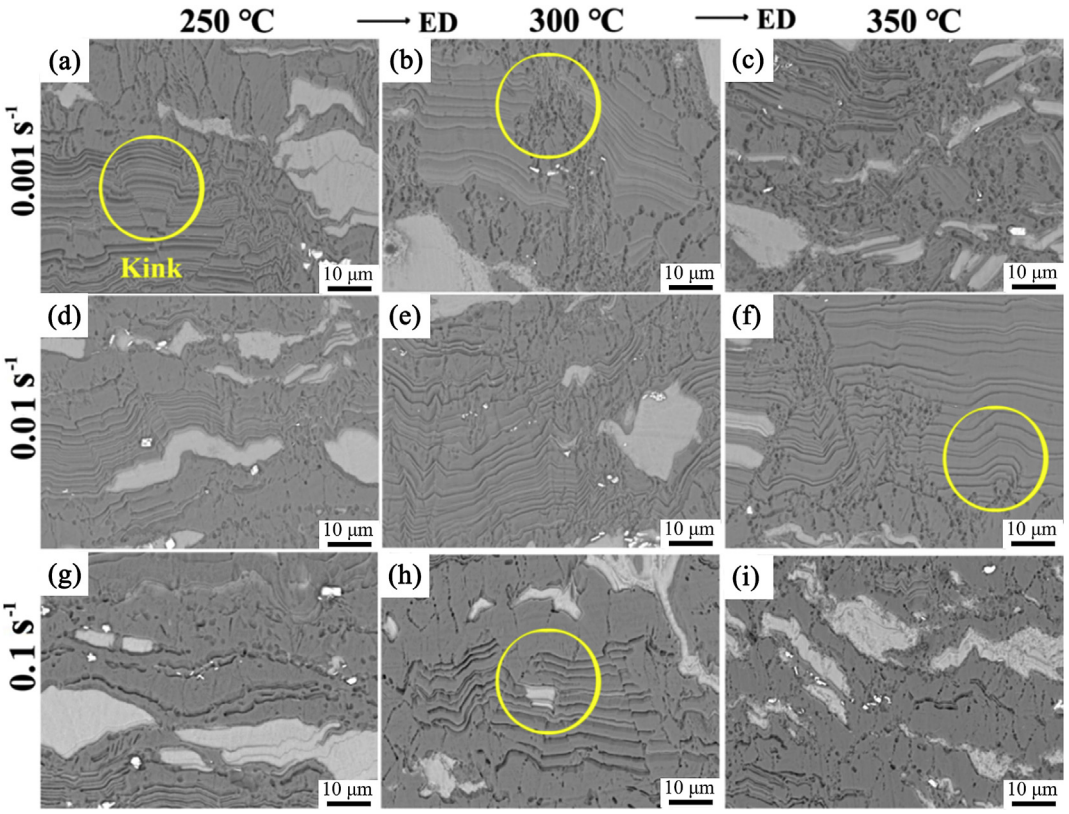

Fig. 9 – SEM microstructural images of VZ 63 alloy after compressive deformations at various temperatures and strain rates.

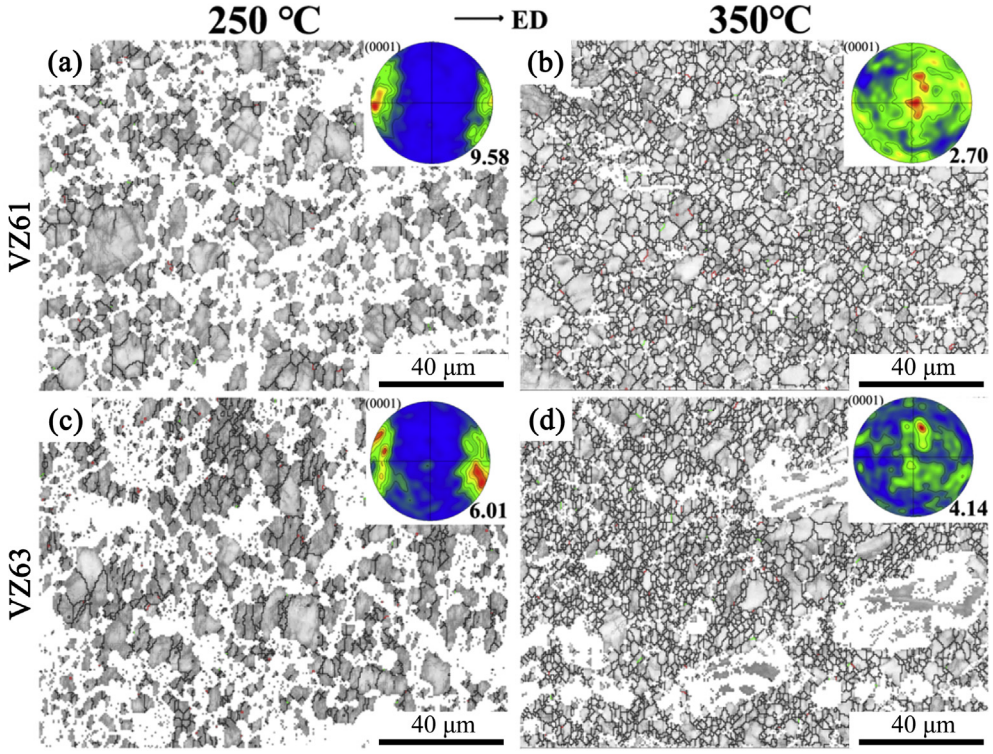

Fig. 10 – EBSD maps of VZ alloys tested at different temperatures with strain rates of 0.001s^{-1}: VZ61 (a) 250 °C, (b) 350 °C, and VZ63: (c) 250 °C, (d) 350 °C.

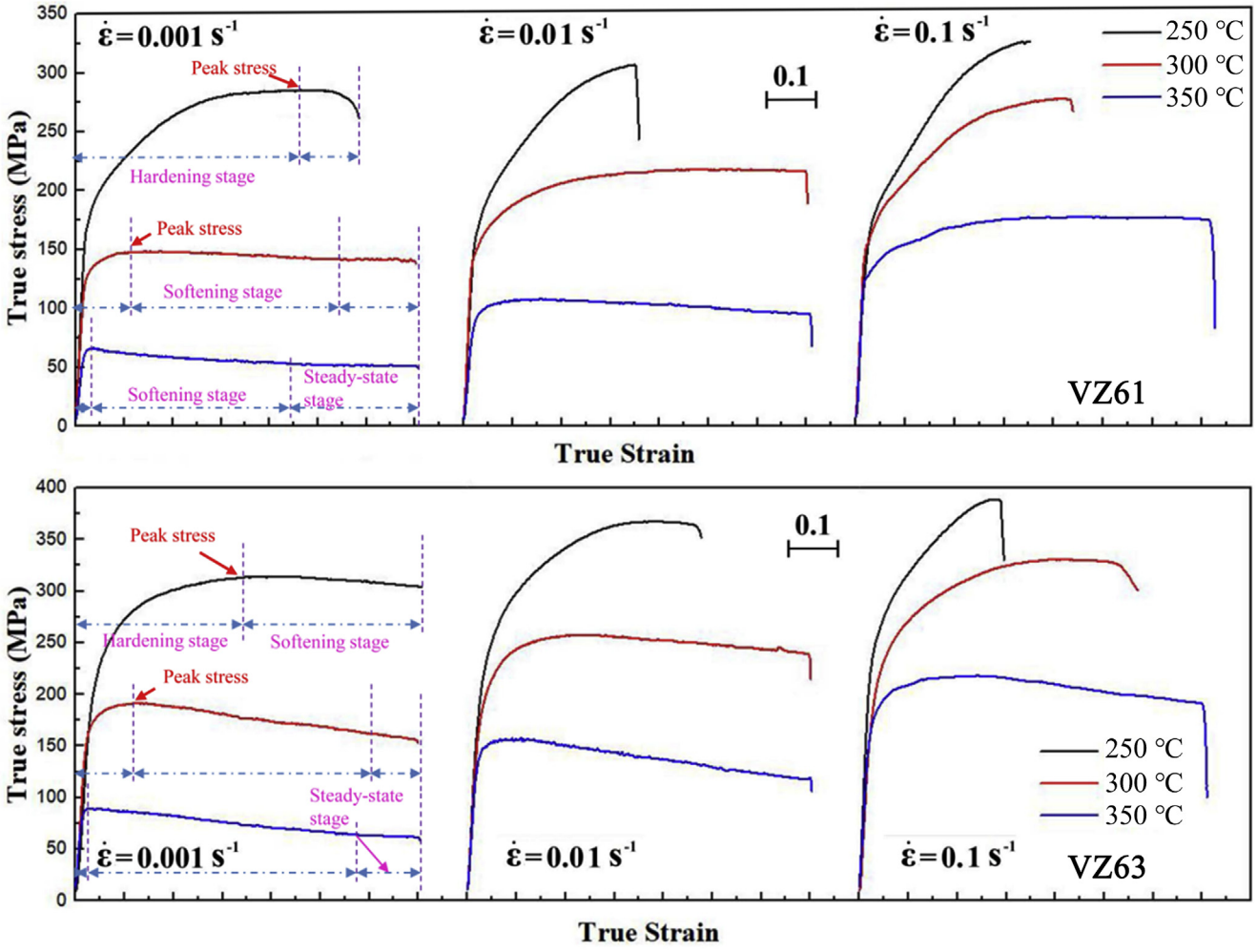

Fig. 11 – True stress–strain curves for the as-extruded alloys at various deformation conditions.

strain hardening, with the increased strain, the gap between the strain hardening and the softening becomes narrower and narrower continuously until it disappears, and then the peak stress is reached. The final softening stage is also classified into two stages:

(1) With further deformation following the peak compressive stress, the deformation tends to be steady owing to the balance between work hardening and recrystallization softening;
(2) The flow stress reduces after peak stress.

The stable stage could not be further observed due to the occurrence of sufficient DRX [46]. In addition, the curves show tiny zigzag characteristics, which is attributed to the dynamic competitive process between strain hardening introduced by dislocation accumulation and recrystallization softening caused by DRX [47]. The compressive peak stress (σ_p) and peak strain (ε_p) under each deformation condition is given in Table 2 and Table 3. The extruded VZ63 alloy has a higher compressive peak stress than VZ61 alloy, regardless of deformation conditions, because the kinked LPSO phase can bear greater external stress. Furthermore, the flow stress gradually

Table 2 – Peak stress (σ_p) and peak strain (ε_p) of as-extruded VZ61 alloy deformed at various deformation.

Alloy	$\dot{\varepsilon}/s^{-1}$	250 °C		300 °C		350 °C	
		σ_p (MPa)	ε_p	σ_p (MPa)	ε_p	σ_p (MPa)	ε_p
VZ61	0.001	284	0.416	147	0.117	65	0.029
	0.01	304	0.342	216	0.430	106	0.135
	0.1	322	0.349	275	0.417	175	0.442

Table 3 – Peak stress (σ_p) and peak strain (ε_p) of as-extruded VZ63 alloy deformed at various deformation.

Alloy	$\dot{\varepsilon}/s^{-1}$	250 °C		300 °C		350 °C	
		σ_p (MPa)	ε_p	σ_p (MPa)	ε_p	σ_p (MPa)	ε_p
VZ63	0.001	314	0.420	192	0.119	90	0.024
	0.01	367	0.378	258	0.226	157	0.201
	0.1	388	0.266	331	0.390	216	0.203

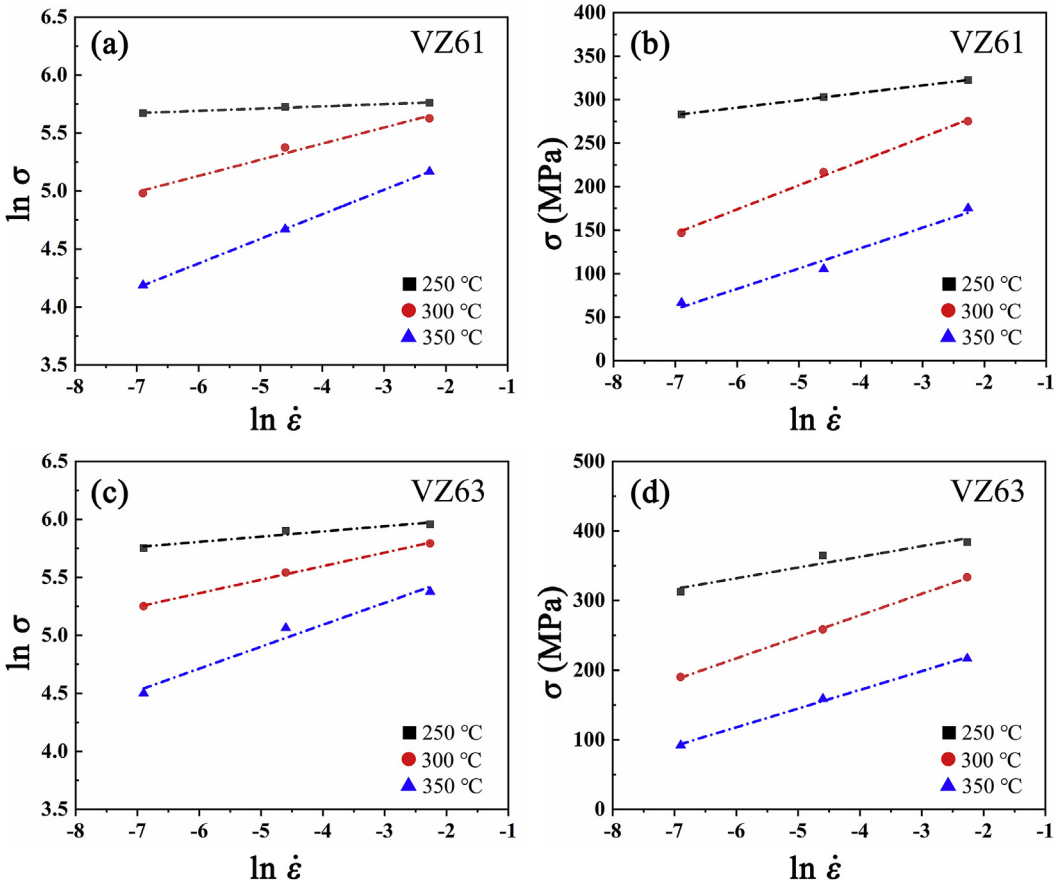

Fig. 12 – Relationship of ln $\dot{\varepsilon}$-lnσ and ln $\dot{\varepsilon}$-σ for VZ alloys.

reduces with the raising of the temperature or reducing strain rate. The strain hardening plays a dominant role in VZ alloys at low temperature, while the dynamic softening gradually becomes obvious with raising the temperature. Meanwhile, the low strain rate can offer enough time for the accumulation of deformation energy, then promoting the dynamic recovery or the nucleation and growth of DRXed grains [48,49].

3.2.3. *Establishment of constitutive equation*

The hot compressive deformation of alloys is closely related to a thermal activation process. In order to better understand the relation among flow tress (σ), strain rate ($\dot{\varepsilon}$) and deformation temperature (T) in VZ alloys during hot deformation, the constitutive equation of flow stress is established based on the Arrhenius equations, as follows [50,51]:

Under low stress levels (ασ < 0.8):

$$\dot{\varepsilon} = A_1 \sigma^{n_1} \exp\left(\frac{-Q}{RT}\right) \tag{2}$$

Under high stress levels (ασ > 1.2) :

$$\dot{\varepsilon} = A_2 \exp(\beta\sigma)\exp\left(\frac{-Q}{RT}\right) \tag{3}$$

As for all stress states it can be expressed according to the hyperbolic line law:

$$\dot{\varepsilon} = A[\sinh(\alpha\sigma)]^n \exp\left(\frac{-Q}{RT}\right) \tag{4}$$

Where α is a stress multiplier, σ is the flow stress (MPa), $\alpha = \beta/n_1$, A_1, A_2, A, β, n_1, n are material constants independent of T. R is the gas constant, R = 8.314 J/mol·K. T is the absolute temperature (K); Q is the deformation activation energy (kJ/mol).

To simplify the equations, natural logarithms were taken of Eqs. (2)–(4), they can then be transformed as:

$$\ln\dot{\varepsilon} = \ln A_1 + n_1 \ln\sigma - \frac{Q}{RT} \tag{5}$$

$$\ln\dot{\varepsilon} = \ln A_2 + \beta\sigma - \frac{Q}{RT} \tag{6}$$

Based on Eqs. (5) and (6), $n_1 = d\ln\dot{\varepsilon}/d\ln\sigma$, $\beta = \ln\dot{\varepsilon}/d\sigma$. The relationships of (ln $\dot{\varepsilon}$-lnσ) and (ln $\dot{\varepsilon}$-σ) at different temperatures are linearly fitted and presented in Fig. 12. The average values of slopes were n_1 and β, respectively. The n_1 values obtained for VZ61 and VZ63 alloys are 16.224 and 11.826, respectively. The β values for VZ61 and VZ63 alloys are 0.066 and 0.044, respectively. The α value of VZ61 and VZ63 alloys obtained by formula $\alpha = \beta/n_1$ are 0.00407 MPa^{-1} and 0.00372 MPa^{-1}, respectively.

Natural logarithms were taken of Eq. (4), it can then be transformed as:

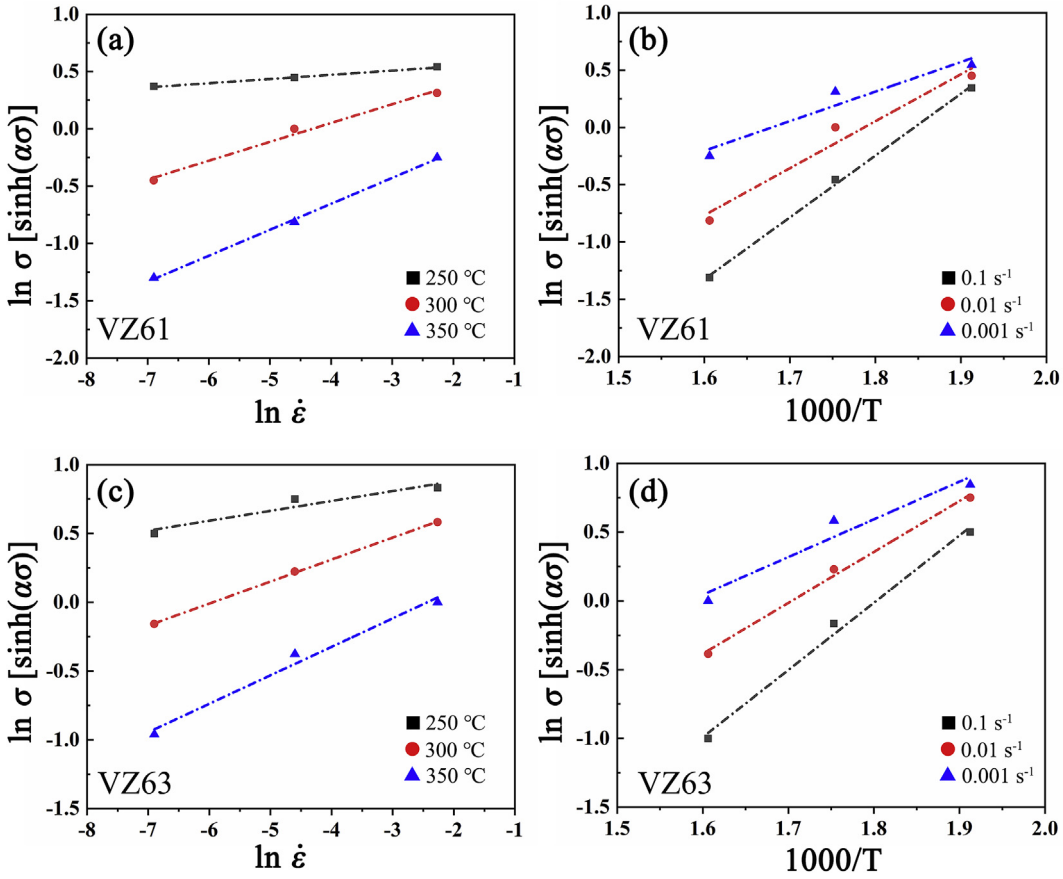

Fig. 13 – Relationships of ln $\dot{\varepsilon}$– ln[sinh(ασ)] and ln[sinh(ασ)] – 1/T for VZ alloys.

$$\ln\dot{\varepsilon} = n\ln[\sinh(\alpha\sigma)] + \ln A - \frac{Q}{RT} \tag{7}$$

If $\dot{\varepsilon}$ is assumed to be a fixed value, and Equation (7) was taken with a partial derivative, the deformation activation energy Q can then be obtained:

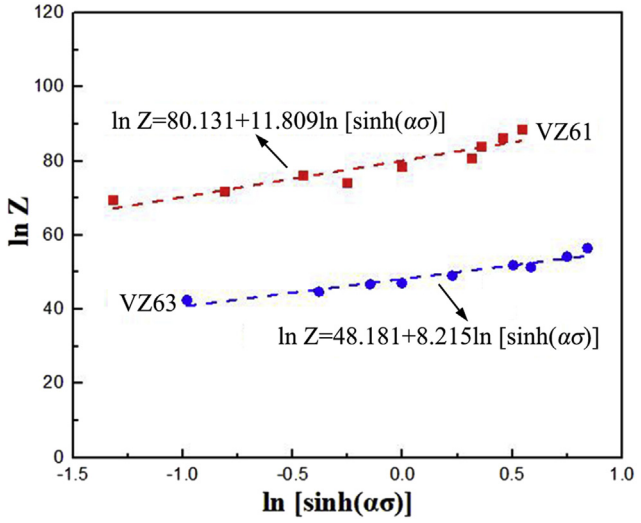

Fig. 14 – Relationship of lnZ –ln[sinh(ασ)] for VZ61 and VZ63 alloys.

$$Q = R\left\{\frac{\partial\ln\dot{\varepsilon}}{\partial\ln[\sinh(\alpha\sigma)]}\right\}_T\left\{\frac{\partial\ln[\sinh(\alpha\sigma)]}{\partial(1/T)}\right\}_{\dot{\varepsilon}} = Rn'S \tag{8}$$

The relationships of (ln $\dot{\varepsilon}$– ln[sinh(ασ)]) and (ln[sinh(ασ)] – 1/T) at various strain rates are fitted and presented in Fig. 13. According to Eq. (8), the values of S and n' are the average value of slopes in (ln $\dot{\varepsilon}$– ln[sinh(ασ)]) and (ln [sinh(ασ)] – 1/T) figures. Thus, the average n' of VZ61 and VZ63 alloys were calculated as 11.809 and 8.215, respectively. The average S of VZ61 and VZ63 alloys is 4.029 and 3.731, respectively. The average activation energy Q of VZ61 and VZ63 alloys could be calculated as 395.5 kJ/mol and 255.6 kJ/mol, respectively. They are not only obviously larger than that for the self-diffusion of pure Mg (135 kJ/mol) [52], but also higher than that for other Mg alloys, such as AZ31 alloy with 161.6 kJ/mol [53,54], extruded Mg-2Gd alloy with about 191 kJ/mol and Mg–Ca alloy with 100–200 kJ/mol [55,56]. The large Q value for VZ alloys is due to the formation of kinked LPSO phase, which can act as a major obstacle to dislocation movement. Although VZ63 alloy has a higher volume fraction of LPSO phase, its Q value is lower than VZ61 alloy, indicating that it is easier to deform thermally. As shown in Fig. 10, compared with VZ61 alloy, VZ63 alloy exhibits finer DRXed grains, because a large number of LPSO particles in VZ63 alloy impede the growth of DRX grains. Thus, finer gains in VZ63 alloy are beneficial for

Table 4 – Values of ε_c and σ_c for the VZ61 alloy.

Alloy	Temperature	Parameter	0.001 s^{-1}	0.01 s^{-1}	0.1 s^{-1}
VZ61	300 °C	ε_c	0.068	0.232	0.290
		σ_c (MPa)	144	208	265
	350 °C	ε_c	0.014	0.065	0.160
		σ_c (MPa)	65	103	164

Table 5 – Values of ε_c and σ_c for the VZ63 alloy.

Alloy	Temperature	Parameter	0.001 s^{-1}	0.01 s^{-1}	0.1 s^{-1}
VZ63	300 °C	ε_c	0.023	0.036	0.289
		σ_c (MPa)	161	204	324
	350 °C	ε_c	0.014	0.014	0.024
		σ_c (MPa)	84	149	185

grain boundary sliding during high temperature deformation, which would decrease the calculated Q value.

The effect of deformation temperature and strain rate on the flow stress is presented based on the Zener-Hollomon parameter, as follows [49,57]:

$$Z = \dot{\varepsilon}\exp\left(\frac{-Q}{RT}\right) = A[sinh(\alpha\sigma)]^n \quad (9)$$

Natural logarithms were taken of Eq. (9), which can be transformed as:

$$\ln Z = \ln\dot{\varepsilon} + \frac{Q}{RT} = n\ln[\sinh(\alpha\sigma)] + \ln A \quad (10)$$

Based on Eq. (10), $n = d\ln Z / d\ln[\sinh(\alpha\sigma)]$, i.e. the slope of $\ln Z - \ln[\sinh(\alpha\sigma)]$ (Fig. 14). It was calculated as 9.807 and 7.403 for VZ61 and VZ63 alloys, respectively. The intercept of the fitted straight line in Fig. 14 is the value of lnA. Thus, A was determined to be 6.316 × 10^{34} and 8.409 × 10^{20} for VZ61 and VZ63 alloys, respectively.

By substituting the calculated parameters A, Q, n and α into Eq. (4), the constitutive equation of flow stress for VZ61 and VZ63 alloys during hot compressive deformation at the temperatures of 250–350 °C and strain rates of 0.001–0.1s^{-1} can then be expressed as follows:

$$\dot{\varepsilon} = 6.316 \times 10^{34}[\sinh(0.00407\sigma)]^{9.807}\exp\left(\frac{-395.567\times10^3}{8.314T}\right) \quad \text{(VZ61 alloy)} \quad (11)$$

$$\dot{\varepsilon} = 8.409 \times 10^{20}[\sinh(0.00372\sigma)]^{7.403}\exp\left(\frac{-255.622\times10^3}{8.314T}\right) \quad \text{(VZ63 alloy)} \quad (12)$$

3.2.4. *DRX kinetic model*

Grain refinement caused by DRX greatly affects the microstructure and properties of Mg alloys. Thus, it is essential to research the effects of various deformation conditions on DRX behavior during the thermal compressive process. According to the constitutive expression, the DRX kinetic models are used for the VZ61 and VZ63 alloys. The recrystallized fraction can be described by the modified Avrami equation, as follows [58,59]:

$$X_{DRX} = 1 - \exp\left[k\left(\frac{\varepsilon-\varepsilon_c}{\varepsilon^*}\right)^n\right] = 1 - \exp\left[k\left(\frac{\varepsilon-\varepsilon_c}{\varepsilon_{0.5}}\right)^n\right] \quad (13)$$

Where X_{DRX} is the volume fraction of DRX grains, ε_c is the critical strain for the initiation of DRX, ε^* the strain for maximum softening rate (replaced by the strain $\varepsilon_{0.5}$, the strain at which the DRX volume fraction is 0.5), n and k are material constants.

The X_{DRX} can be estimated as [60]:

$$X_{DRX} = \frac{\sigma_p - \sigma}{\sigma_p - \sigma_{ss}} = 1 - \exp\left[k\left(\frac{\varepsilon-\varepsilon_c}{\varepsilon_{0.5}}\right)^n\right] \quad (14)$$

Where σ_p is the peak stress, σ_{ss} is the steady-state stress of DRX. They are achieved by evaluating the strain hardening rate θ - σ curve [60,61], then substituting the values of σ_p, σ_{ss}, ε_c and $\varepsilon_{0.5}$ under various deformation conditions into Eq. (14), the average value of k and n can be obtained, k (VZ61) = - 0.876, n (VZ61) = 1.419; k (VZ63) = - 0.819, n (VZ63) = 1.775. Thus, the X_{DRX} of VZ alloys can be presented as:

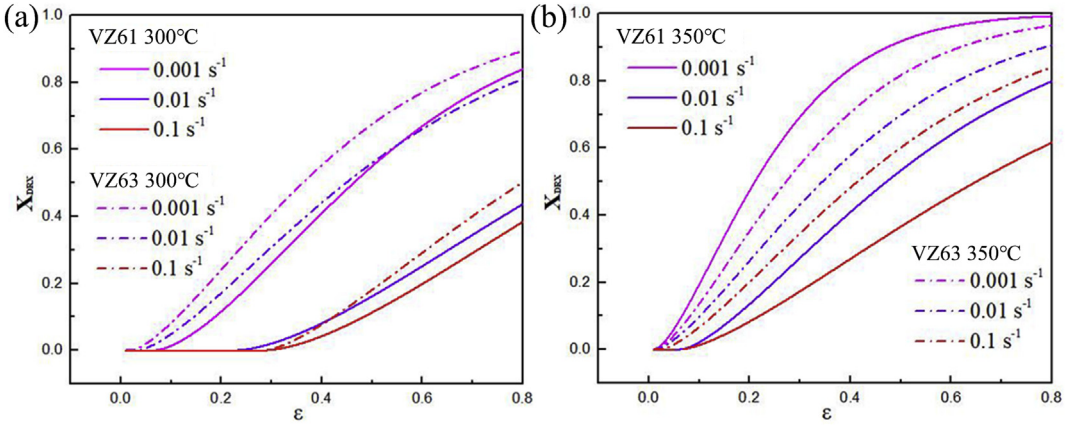

Fig. 15 – X_{DRX} of the VZ alloy at various deformation parameters.

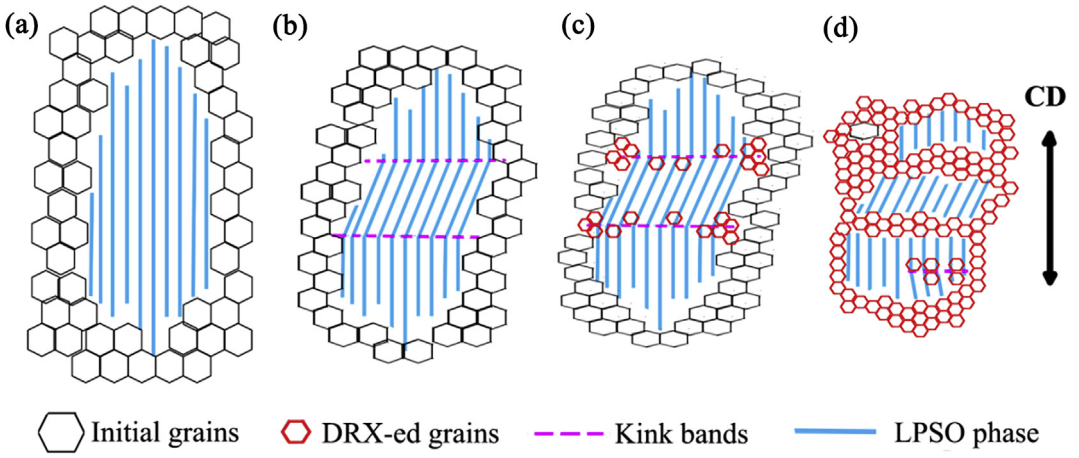

Fig. 16 – Schematic illustrations to show the LPSO phase evolution during compression at elevated temperature.

$$X_{DRX} = 1 - \exp\left[-0.87606\left(\frac{\varepsilon - \varepsilon_c}{\varepsilon^*}\right)^{1.419}\right] \quad \text{(VZ61 alloy)} \tag{15}$$

$$X_{DRX} = 1 - \exp\left[-0.81978\left(\frac{\varepsilon - \varepsilon_c}{\varepsilon^*}\right)^{1.776}\right] \quad \text{(VZ63 alloy)} \tag{16}$$

Tables 4 and 5 show the ε_c and σ_c values of the VZ alloys at various deformation conditions. The ε_c value of VZ alloys decreases with the raising of the deformation temperature and the decreasing of the strain rate. As for VZ63 alloy, such evolutions are much more obvious, indicating that DRX behavior occurs more easily in VZ63 alloy than that in VZ61 alloy.

The X_{DRX} of VZ61 and VZ63 alloys under different deformation parameters calculated by Eqs. (15) and (16) is shown in Fig. 15. At 300 °C (Fig. 15a), the X_{DRX} of VZ61 and VZ63 alloys decreases with the increase of strain rate. Since recrystallization was a slow continuous process, it could not respond quickly to coordinated deformation with increasing the strain rate. Low strain rate could offer enough time for accumulation deformation energy, which is conducive to nucleation and growth of DRXed grains. In addition, the VZ63 alloy possess higher X_{DRX} than VZ61 alloy at the same strain rate, indicating that the increase of LPSO phase in VZ63 alloy is beneficial for the occurrence of dynamic recrystallization. In section 3.1.2, it was discussed that the accumulation of dislocation is easier to occur around the kinked LPSO phase (as shown in Fig. 6), which can accelerate DRX nucleation in VZ63 alloy during high temperature deformation. This is also the reason why the average activation energy Q of VZ63 is lower than that of VZ61 alloy during hot deformation. When the deformation temperature rises to 350 °C (Fig. 15b), the X_{DRX} of VZ61 and VZ63 alloys further increases, which is in good agreement with the results shown in Figs. 8 and 9. Higher dislocation mobility and more activated non-basal slip occurred as raising temperature, promoting the nucleation and growth of DRXed grains [62].

For better illustration, the simplified models (Fig. 16) were established to describe the LPSO phase evolution during compression at elevated temperature. During the compression process, the LPSO phases first kinked (Fig. 16b), which easily result in stress concentrations at grain and kink boundaries, thus, it can be expected that recrystallization nucleates near these interfaces. As DRX expands at the kink bands (Fig. 16c), the initial coarse deformed grains are divided into several parts and formation of kink bands can change the grain orientation, and promote the activation of the basal slip during the continuous loading process. With the compressive strain further increasing (Fig. 16d), the kinking and DRX continues to occur in the separated deformed grains, leading to the increase of recrystallization volume fraction, and the microstructural homogenization.

4. Conclusions

Compressive deformation of as-extruded LPSO-containing Mg alloys were investigated by uniaxial compressive experiments at various temperatures and strain rates. The Arrhenius equation was developed on the basis of the true stress–strain curves. The DRX kinetic model was developed and verified. The following conclusions were drawn:

(1) Block LPSO phase and thin-platelet LPSO phase existed in VZ alloys. The former had 14H structure and the latter 18R structure. Both the morphologies of these two LPSO phases exhibited obvious kink deformations during compressive deformation.
(2) During room temperature compression, since numerous dislocations were accumulated around the kinked LPSO phases, which can hinder dislocation movement, the compressive yield strength of VZ63 alloy with more LPSO phase was obviously improved. In addition, the VZ63 alloy also exhibited a higher strain hardening rate than VZ61 alloy at stage III, which was related to the fact that more LPSO phase inVZ63 alloy can bear greater external stress and improve the deformation resistance. However, the activation of

more twining was beneficial for improving the hardening strain rate at stage II for VZ61 alloy.

(3) During high temperature compression, the true stress–strain curves showed that the flow stress gradually reduced with increasing temperature and also the reducing of strain rate, due to the occurrence of dynamic recrystallization (DRX). The VZ63 alloy displayed a higher peak stress than VZ61 alloy due to the existence of more LPSO phase. In addition, compared with the VZ61 alloy, the VZ63 alloy exhibited a lower Q value, since a large number of LPSO particles in VZ63 alloy impeded the growth of DRX grains, which were beneficial for grain boundary sliding during high temperature deformation and decreased the calculated Q value. The DRX kinetic models also indicated that the VZ63 alloy was more prone to DRX with a higher volume fraction of dynamically recrystallized grains (X_{DRX}) at the same deformation conditions. The reason was that more dislocation accumulation around the kinked LPSO phase can accelerate DRX nucleation in VZ63 alloy at high temperatures.

Declaration of Competing Interest

The authors declare that they have no known competing financial interests or personal relationships that could have appeared to influence the work reported in this paper.

Acknowledgments

The authors thank the National Natural Science Foundation of China (No. 52171103), and Fundamental Research Funds for the Central Universities (No. 2020CDJDPT001) for the financial supports. The China Scholarship Council is also gratefully acknowledged for financial support for Di Zhao (202006050158).

REFERENCES

[1] Bazhenov VE, Li AV, Komissarov AA, Koltygin AV, Tavolzhanskii SA, Bautin VA, et al. Microstructure and mechanical and corrosion properties of hot-extruded Mg-Zn-Ca-(Mn) biodegradable alloys. J. Magnes Alloys 2021;9:1428–42.

[2] Liu CQ, Chen XH, Chen J, Atrens A, Pan FS. The effects of Ca and Mn on the microstructure, texture and mechanical properties of Mg-4 Zn alloy. J. Magnes Alloys 2021;9:1084–97.

[3] Sabat RK, Brahme AP, Mishra RK, Inal K, Suwas S. Ductility enhancement in Mg-0.2%Ce alloys. Acta Mater 2018;161:246–57.

[4] Hwang JH, Zargaran A, Park G, Lee O, Lee BJ, Kim NJ. Effect of 1Al addition on deformation behavior of Mg. J. Magnes Alloys 2021;9:489–98.

[5] Shi BQ, Xiao YH, Shang XL, Cheng YQ, Yan H, Dong Y, et al. Achieving ultra-low planar anisotropy and high stretch formability in a Mg-1.1Zn-0.76Y-0.56Zr sheet by texture tailoring via final-pass heavy reduction rolling. Mater Sci Eng, A 2019;746:115–26.

[6] Somekawa H, Kinoshita A, Kato A. Effect of alloying elements on room temperature stretch formability in Mg alloys. Mater Sci Eng, A 2018;732:21–8.

[7] Liu XQ, Qiao XG, Pei RS, Chi YQ, Yuan L, Zheng MY. Role of extrusion rate on the microstructure and tensile properties evolution of ultrahigh-strength low-alloy Mg-1.0Al-1.0Ca-0.4Mn (wt.%) alloy. J Magnes Alloys 2021. https://doi.org/10.1016/j.jma.2021.05.010.

[8] Wang SH, Ma JF, Yang JL, Zhang WC, Sun Y, Pan J, et al. Improving the ductility of Mg-2.5Nd-0.5Zn-0.5Zr alloy by multi-pass hot rolling. J Mater Res Technol 2021;14:2124–30.

[9] He C, Zhu HR, Yuan M, Jiang B, Wang QH, Chai YF, et al. Comparison of room-temperature stretch formability of the as extruded Mg-Gd alloys with different double-peak pole spacing. J Mater Res Technol 2021;15:4838–51.

[10] Zhang Y, Rong W, Wu YJ, Peng LM. Achieving ultra-high strength in Mg-Gd-Ag-Zr wrought alloy via bimodal-grained structure and enhanced precipitation. J Mater Sci Technol 2020;54:160–70.

[11] Liu P, Jiang HT, Cai ZX, Kang Q, Zhang Y. The effect of Y, Ce and Gd on texture, recrystallization and mechanical property of Mg-Zn alloys. J. Magnes. Alloys 2016;4:188–96.

[12] Zhao Y, Zhang DF, Xu JY, Zhong SY, Jiang B, Pan FS. A good balance between strength and ductility in Mg–Zn-Mn-Gd alloy. Intermetallics 2021;132:107163.

[13] Zheng J, Yan Z, Ji J, Shi Y, Zhang H, Zhang Z, et al. Effect of heat treatment on mechanical properties and microstructure evolution of Mg-9.5Gd-4Y-2.2Zn-0.5Zr alloy. J. Magnes. Alloys 2021. https://doi.org/10.1016/j.jma.2021.05.018.

[14] Ashrafizadeh SM, Mahmudi R, Geranmayeh AR. A comparative study on the effects of Gd, Y and La rare-earth elements on the microstructure and creep behavior of AZ81 Mg alloy. Mater Sci Eng, A 2020;790:139712.

[15] Zhu J, Chen JB, Liu T, Liu JX, Wang WY, Liu ZK, et al. High strength Mg 94 Zn 2.4 Y 3.6 alloy with long period stacking ordered structure prepared by near-rapid solidification technology. Mater Sci Eng, A 2017;679:476–83.

[16] Chen X, Ning S, Wang A, Le Q, Liao Q, Jia Y, et al. Microstructure, mechanical properties and corrosion behavior of quasicrystal-reinforced Mg-Zn-Y alloy subjected to dual-frequency ultrasonic field. Corrosion Sci 2020;163:108289.

[17] Tahreen N, Zhang DF, Pan FS, Jiang XQ, Li DY, Chen DL. Strengthening mechanisms in magnesium alloys containing ternary I, W and LPSO phases. J Mater Sci Technol 2018;34:1110–8.

[18] Ye X, Cao HS, Qi FG, Ouyang XP, Ye ZS, Hou CH, et al. Effect of Y Addition on the microstructure and mechanical properties of ZM31 alloy. Materials 2020;13:853.

[19] Su N, Xue X, Zhou H, Wu Y, Deng Q, Yang K, et al. Effects of nanoprecipitates and LPSO structure on deformation and fracture behaviour of high-strength Mg-Gd-Y-Zn-Mn alloys. Mater Char 2020;165:110396.

[20] Wang D, Wu H, Wu R, Wang Y, Zhang J, Betsofen S, et al. The transformation of LPSO type in Mg-4Y-2Er-2Zn-0.6Zr and its response to the mechanical properties and damping capacities. J. Magnes. Alloys 2020;8:793–8.

[21] Hao J, Zhang J, Li B, Xie R. Effects of 14H LPSO phase on the dynamic recrystallization and work hardening behaviors of an extruded Mg-Zn-Y-Mn alloy. Mater Sci Eng, A 2021;804:140727.

[22] Hagihara K, Li Z, Yamasaki M, Kawamura Y, Nakano T. Strengthening mechanisms acting in extruded Mg-based long-period stacking ordered (LPSO)-phase alloys. Acta Mater 2019;163:226–39.

[23] Wang D, Ma XC, Wu RZ, Wu HJ, Wang JH, Zhang S, et al. Effect of extrusion plus rolling on damping capacity and mechanical properties of Mg-Y-Er-Zn-Zr alloy. Mater Sci Eng, A 2022;830:142298.
[24] Li K, Chen Z, Chen T, Shao J, Wang R, Liu C. Hot deformation and dynamic recrystallization behaviors of Mg-Gd-Zn alloy with LPSO phases. J Alloys Compd 2019;792:894–906.
[25] Hagihara K, Yokotani N, Umakoshi Y. Plastic deformation behavior of Mg12YZn with 18R long-period stacking ordered structure. Intermetallics 2010;18:267–76.
[26] Wang K, Wang J, Peng X, Gao S, Hu H, Zeng L, et al. Microstructure and mechanical properties of Mg-Gd-Y-Zn-Mn alloy sheets processed by large-strain high-efficiency rolling. Mater Sci Eng, A 2019;748:100–7.
[27] Yamasaki M, Anan T, Yoshimoto S, Kawamura Y. Mechanical properties of warm-extruded Mg-Zn-Gd alloy with coherent 14H long periodic stacking ordered structure precipitate. Scripta Mater 2005;53:799–803.
[28] Wang J, Gao S, Liu X, Peng X, Wang K, Liu S, et al. Enhanced mechanical properties and degradation rate of Mg–Ni–Y alloy by introducing LPSO phase for degradable fracturing ball applications. J. Magnes. Alloys 2020;8:127–33.
[29] Garces G, Perez P, Cabeza S, Lin HK, Kim S, Gan W, et al. Reverse tension/compression asymmetry of a Mg-Y-Zn alloys containing LPSO phases. Mater Sci Eng, A 2015;647:287–93.
[30] Zhao SS, Lin XP, Dong Y, Niu Y, Xu D, Sun H. High-temperature tensile properties and deformation mechanism of polycrystalline magnesium alloys with specifically oriented columnar grain structures. Mater Sci Eng, A 2018;729:300–9.
[31] Kondori B, Mahmudi R. Effect of Ca additions on the microstructure, thermal stability and mechanical properties of a cast AM60 magnesium alloy. Mater Sci Eng, A 2010;527:2014–21.
[32] Movahedi-Rad A, Mahmudi R. Effect of Ag addition on the elevated-temperature mechanical properties of an extruded high strength Mg-Gd-Y-Zr alloy. Mater Sci Eng, A 2014;614:62–6.
[33] Luo AA. Recent magnesium alloy development for elevated temperature applications. Mater Rev 2004;49:13–30.
[34] Wen D, Yangshan S, Xuegang M, Feng X, Min Z, Dengyun W. Microstructure and mechanical properties of Mg-Al based alloy with calcium and rare earth additions. Mater Sci Eng, A 2003;356:1–7.
[35] Garcés G, Oñorbe E, Dobes F, Pérez P, Antoranz JM, Adeva P. Effect of microstructure on creep behaviour of cast Mg97Y2Zn1 (at.%) alloy. Mater Sci Eng, A 2012;539:48–55.
[36] Kekule T, Smola B, Vlach M, Kudrnova H, Kodetova V, Stulikova I. Thermal stability and microstructure development of cast and powder metallurgy produced Mg-Y-Zn alloy during heat treatment. J. Magnes. Alloys 2017;5:173–80.
[37] Hagihara K, Kinoshita A, Sugino Y, Yamasaki M, Kawamura Y, Yasuda HY, et al. Effect of long-period stacking ordered phase on mechanical properties of Mg97Zn1Y2 extruded alloy. Acta Mater 2010;58:6282–93.
[38] Chen T, Chen Z, Shao J, Wang R, Mao L, Liu C. The role of long period stacking ordered phase in dynamic recrystallization of a Mg–Zn–Y alloy during hot compression. J Alloys Compd 2020;818:152814.
[39] Kocks UF, Mecking H. Physics and phenomenology of strain hardening: the FCC case. Prog Mater Sci 2003;48:171–273.
[40] Zhao C, Li Z, Shi J, Chen X, Tu T, Luo Z, et al. Strain hardening behavior of Mg-Y alloys after extrusion process. J. Magnes. Alloys 2019;7:672–80.
[41] Wang B, Wang F, Wang Z, Zhou L, Liu Z, Mao P. Compressive deformation behavior of ultrafine-grained Mg-3Zn-1.2Ca-0.6Zr alloy at room temperature. J Alloys Compd 2021;871:159581.
[42] Xu SW, Kamado S, Matsumoto N, Honma T, Kojima Y. Recrystallization mechanism of as-cast AZ91 magnesium alloy during hot compressive deformation. Mater Sci Eng, A 2009;527:52–60.
[43] Zhang L, Han Y. Twins formation and their role in nanostructuring of zirconium. Mater Sci Eng, A 2009;523:130–3.
[44] Sarker D, Chen DL. Detwinning and strain hardening of an extruded magnesium alloy during compression. Scripta Mater 2012;67:165–8.
[45] Xu Y, Chen C, Zhang X, Dai H, Jia J, Bai Z. Dynamic recrystallization kinetics and microstructure evolution of an AZ91D magnesium alloy during hot compression. Mater Char 2018;145:39–52.
[46] Xia X, Chen Q, Huang S, Lin J, Hu C, Zhao Z. Hot deformation behavior of extruded Mg-Zn-Y-Zr alloy. J Alloys Compd 2015;644:308–16.
[47] Cai Z, Chen F, Guo J. Constitutive model for elevated temperature flow stress of AZ41M magnesium alloy considering the compensation of strain. J Alloys Compd 2015;648:215–22.
[48] Liu Z, Huang T, Liu Wj, Kang S. Dislocation mechanism for dynamic recrystallization in twin-roll casting Mg-5.51Zn-0.49Zr magnesium alloy during hot compression at different strain rates. Trans Nonferrous Metals Soc China 2016;26:378–89.
[49] Quan GZ, Shi Y, Wang YX, Kang BS, Ku TW, Song WJ. Constitutive modeling for the dynamic recrystallization evolution of AZ80 magnesium alloy based on stress–strain data. Mater Sci Eng, A 2011;528:8051–9.
[50] Wang Z, Qi L, Wang G, Li H, Dargusch MS. Constitutive equation for the hot deformation behavior of Csf/AZ91D composites and its validity for numerical simulation. Mech Mater 2016;102:90–6.
[51] Wang T, Chen Y, Ouyang B, Zhou X, Hu J, Le Q. Artificial neural network modified constitutive descriptions for hot deformation and kinetic models for dynamic recrystallization of novel AZE311 and AZX311 alloys. Mater Sci Eng, A 2021;816:141259.
[52] Frost HJ, Ashby MF. Deformation-mechanism maps. Oxford: Pergamon Press; 1982.
[53] Arun MS, Chakkingal U. A constitutive model to describe high temperature flow behavior of AZ31B magnesium alloy processed by equal-channel angular pressing. Mater Sci Eng, A 2019;754:659–73.
[54] Liu J, Cui Z, Li C. Modelling of flow stress characterizing dynamic recrystallization for magnesium alloy AZ31B. Comput Mater Sci 2008;41:375–82.
[55] Hoseini-Athar MM, Mahmudi R. Effect of Zn content on hot deformation behavior of extruded Mg-Gd-Zn alloys. Mater Sci Eng, A 2019;759:745–53.
[56] Papillon J, Salero P, Mercier F, Fabrègue D, Maire É. Compressive deformation behavior of dendritic Mg-Ca(-Zn) alloys at high temperature. Mater Sci Eng, A 2019;763:138180.
[57] Yao Y, Liu C, Wan Y, Yu S, Gao Y, Jiang S. Microstructure, texture and mechanical anisotropy of Mg-Gd-Y-Zr sheets processed via different rolling routes and reductions. Mater Char 2020;161:110120.
[58] Lv BJ, Peng J, Wang YJ, An XQ, Zhong LP, Tang AT, et al. Dynamic recrystallization behavior and hot workability of Mg-2.0Zn-0.3Zr-0.9Y alloy by using hot compression test. Mater Des 2014;53:357–65.

[59] Hao J, Zhang J, Xu C, Nie K. Optimum parameters and kinetic analysis for hot working of a solution-treated Mg-Zn-Y-Mn magnesium alloy. J Alloys Compd 2018;754:283–96.
[60] Poliak EI, Jonas JJ. A one-papameter approach to determining the critical conditons for the initiation of dynamic recrystallization. Acta Mater 1993;44:127–36.
[61] Chen MS, Lin YC, Ma X-S. The kinetics of dynamic recrystallization of 42CrMo steel. Mater Sci Eng, A 2012;556:260–6.
[62] Ou L, Nie Y, Zheng Z. Strain compensation of the constitutive equation for high temperature flow stress of a Al-Cu-Li alloy. J Mater Eng Perform 2013;23:25–30.